

# Internally heated porous convection: an idealised model for Enceladus' hydrothermal activity

Thomas Le Reun <sup>1</sup> and Duncan R. Hewitt <sup>2</sup>

<sup>1</sup>DAMTP, University of Cambridge, Wilberforce Road, Cambridge CB3 0WA, UK

<sup>2</sup>Department of Mathematics, University College London, UK

## Key Points:

- We carry out numerical and theoretical analysis of an idealised model of tidally driven hydrothermal activity inside Enceladus.
- With numerical and theoretical analysis, we explore the flow that develops in a porous core with volumetric heating.
- Our model allows us to predict typical temperature, velocity and heat flux anomalies at the bottom of Enceladus' subsurface ocean.

---

Corresponding author: Thomas Le Reun, [t1402@cam.ac.uk](mailto:t1402@cam.ac.uk)

## Abstract

Recent planetary data and geophysical modelling suggest that hydrothermal activity is ongoing under the ice crust of Enceladus, one of Saturn’s moons. According to these models, hydrothermal flow in the porous, rocky core of the satellite is driven by tidal deformation that induces dissipation and volumetric internal heating. Despite the effort in the modelling of Enceladus’ interior, systematic understanding—and even basic scaling laws—of internally-heated porous convection and hydrothermal activity are still lacking. In this article, using an idealised model of an internally-heated porous medium, we explore numerically and theoretically the flows that develop close and far from the onset of convection. In particular, we quantify heat-transport efficiency by convective flows as well as the typical extent and intensity of heat-flux anomalies created at the top of the porous layer. With our idealised model, we derive simple and general laws governing the temperature and hydrothermal velocity that can be driven in the oceans of icy moons. In the future, these laws could help better constraining models of the interior of Enceladus and other icy satellites.

## Plain Language Summary

Enceladus, one of Saturn’s icy moons, is known from planetary data to be the site of ongoing hydrothermal activity. According to recent modelling, this activity is driven by tidal distortion throughout its porous rocky core, which causes friction and induces volumetric heating. As subsurface water penetrates through the core, it warms, rises, and returns into the ocean through localised hotspots. We introduce an idealized model of this hydrothermal circulation in order to understand the formation of hot spots, their typical size and their activity. We find that the hydrothermal flow in the porous core of Enceladus is about a few centimetres per year and is thus much slower than circulations in the Earth’s ocean crust. As a result, the timescale for hotspot activity variations is as long as a few million years. Despite the slowness of the circulation, we predict that it drives oceanic plumes with velocity of the order of one centimetre per second.

## 1 Introduction

Enceladus, a 500 km-diameter icy satellite orbiting Saturn, has drawn a lot of attention since the first flybys operated by the Cassini probe in 2005. Pictures and *in situ* astrochemical measurement have revealed the presence of a water-vapour and ice plume ejected into outer space. It emerges along fractures in the ice crust at the south pole of Enceladus and is associated with a large heat-flux anomaly of 12.5 GW (Spencer et al., 2006, 2018). Subsequent analyses have revealed that the ejected material contains silicate particles of nanometric size whose chemistry indicates that the water contained in the plume has been previously hot, liquid, and in contact with silicate rocks (Hsu et al., 2015; Sekine et al., 2015). Enceladus’ plumes have since then been interpreted as evidence for hydrothermal activity occurring below the ice crust of Enceladus. This is a surprising implication because, unlike the Earth, Enceladus has radiated away all its initial heat, and its small size makes internal heating by radiogenic elements insufficient to explain the abnormal heat flux (Nimmo & Pappalardo, 2016; Choblet et al., 2017).

Building on the recent study of Lainey et al. (2017), Choblet et al. (2017) have recently proposed a self-consistent model to explain the hydrothermal activity based on internal heating by tides in Enceladus’ water-saturated porous core. This model relies on recent findings regarding the interior of Enceladus. Underneath its ice crust, this satellite comprise a global subsurface ocean, with thickness varying from 30 to 50 km (Thomas et al., 2016). Below lies a core made of rocky material that remains undifferentiated and uncompactd owing to to the weakness of Enceladus’ gravity field (Roberts, 2015; Choblet et al., 2017). The core is thus permeated with the water of the ocean; Choblet et al. (2017) estimate that the porosity ranges from 20 to 30% for a water-filled rocky core. Lastly,

63 intense internal heating (Lainey et al., 2017) due to tidally-induced deformation and fric-  
 64 tion heats the water and creates a porous flow with hot and narrow upwelling zones, pos-  
 65 sibly leading to hot spots of water flowing into the ocean (Choblet et al., 2017).

66 Hydrothermal convection with internal heating is only a relatively recent feature  
 67 of thermal evolution models (Travis et al., 2012; Travis & Schubert, 2015), and it is in  
 68 general driven by radiogenic heating or serpentinisation rather than tidal deformation  
 69 (Nimmo & Pappalardo, 2016). However, interior models of icy moons deal with very poorly  
 70 constrained parameters, for instance the permeability of the core for which a range of  
 71 orders of magnitudes is plausible (Travis & Schubert, 2015; Choblet et al., 2017). De-  
 72 spite systematic studies covering a wide range of parameters (Choblet et al., 2017), gen-  
 73 eral scaling laws predicting the size and intensity of heat-flux anomalies, the typical tem-  
 74 perature or hydrothermal velocity and their dependence to physical parameters are still  
 75 lacking. By investigating a basic model for internally-heated porous convection, we aim  
 76 to derive these scaling laws, which could prove useful to better constrain the planetary  
 77 data available for Enceladus or to build thermal-evolution models of icy moons more gen-  
 78 erally (Travis et al., 2012; Travis & Schubert, 2015).

79 In the present article, we thus explore systematically internally-heated porous con-  
 80 vection close to and far from the onset of motion with numerical simulations and math-  
 81 ematical analysis. We use an idealised two-dimensional Cartesian model of a water-saturated  
 82 porous layer with internal heating in order to reduce the complexity of the system as much  
 83 as possible while retaining the key physical ingredients, which are internal heating and  
 84 an open-top boundary. This kind of approach has a long history of use in convection stud-  
 85 ies. The canonical model to study heat transport by convection is the Rayleigh-Bénard  
 86 set-up (a confined porous layer heated from below and cooled from the top) which has  
 87 received a significant amount of study (Otero et al., 2004; Hewitt et al., 2012, 2014; He-  
 88 witt & Lister, 2017). The more closely related case of Earth-like hydrothermal systems  
 89 with a bottom heat flux and open top boundary has also been widely studied (see for  
 90 instance Fontaine and Wilcock (2007); Coumou et al. (2008, 2009)). However, the re-  
 91 sults of these investigations are unlikely to apply to tidally-driven hydrothermal circula-  
 92 tion because of either unsuitable boundary condition or the nature of the heat source.  
 93 Very few systematic experimental and numerical studies have been devoted to internally-  
 94 heated porous convection. Those that have are focused mostly on the onset of motion  
 95 and average heat transport (Burette & Berman, 1976; Nield & Kuznetsov, 2013; Hardee  
 96 & Nilson, 1977; Kulacki & Ramchandani, 1975). Hence, these studies do not allow the  
 97 derivation of scalings governing, for instance, the typical extent of upwelling zones or the  
 98 associated thermal anomalies and fluid velocities, in the case of tidally-driven hydrother-  
 99 mal activity. That is our aim here.

100 In common with numerous convection set-ups, we find that the intensity of heat-  
 101 transporting motion is characterised by only one dimensionless number, the Rayleigh num-  
 102 ber, noted  $Ra$ , which increases with volumetric heat production, permeability and core  
 103 radius. Performing numerical simulations and asymptotic analysis, we find that the typ-  
 104 ical size of thermal anomalies is proportional to  $Ra^{-1/2}$ , owing to a balance between ad-  
 105 vection, heat production and advection. As a consequence, the plumes driven in the ocean  
 106 by thermal anomalies have a buoyancy scaling like  $Ra^{3/2}$ . When quantified for ranges  
 107 of parameters that are expected for Enceladus, we predict typical Darcy fluxes in the core  
 108 of at most 10 cm per year, while hydrothermal velocities are expected to reach about 1  
 109  $\text{cm.s}^{-1}$ .

110 This paper is organised as follows. A first part is devoted to introducing our ide-  
 111 alised model for an internally-heated, saturated porous layer and identifying the rele-  
 112 vant dimensionless parameters. We then carry out a stability analysis to determine the  
 113 conditions under which convection happens. Afterwards, we describe and analyse nu-  
 114 merical simulations of internally-heated porous convection, focusing in particular on the  
 115 structure of the flow and the associated thermal anomalies. Lastly, we apply the laws

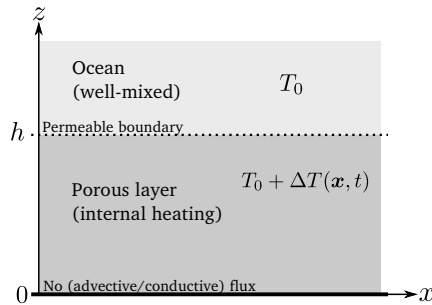


**Figure 1.** An idealised two-dimensional model to describe porous convection inside core in interaction with the subsurface ocean in an icy moon of the type of Enceladus. The bottom of the porous layer models the centre of the moon, there is no heat and mass flux at this height. Mass exchange between the ocean and the porous core are allowed with a free vertical velocity at the top.

116 derived from our idealised model to Enceladus to quantify the temperature anomalies  
117 and the typical hydrothermal velocities that can be induced in its ocean.

## 118 2 A simple model for the interior of icy moons

### 119 2.1 The model and its governing equations

120 We consider an idealised model of tidally-driven convection inside icy moons of the  
121 type of Enceladus to focus on the effect of two fundamental ingredients: internal heat-  
122 ing and an open top boundary. We thus make a series of simplifying approximations.  
123 First, rather than modelling the full fluid system, comprising the water-saturated core  
124 and the ocean, we consider only the core, and we parametrise the core–ocean interac-  
125 tion via boundary conditions that will be specified below. Second, we consider a two-  
126 dimensional Cartesian model instead of modelling a full sphere. Third, we treat the grav-  
127 itational field as constant in space, although it should increase away from the centre of  
128 the moon, and we consider either constant or horizontally varying internal heat gener-  
129 ation, although it, too, should vary with depth. We treat all other parameters, includ-  
130 ing the permeability, as constants. We will return in section 6 to consider and discuss  
131 the effect of some of these assumptions, as we apply our general findings and scalings  
132 to the case of Enceladus.

We thus consider a two-dimensional porous core of (uniform) permeability  $k$ , which is saturated with water of viscosity  $\mu$ . It lies beneath an ocean that we assume to be well mixed with a global temperature  $T_0$  (see figure 1). The volume (or Darcy) flux  $\mathbf{U} = (U, W)$  inside the porous core is modelled by Darcy’s law,

$$\mathbf{U} = \frac{k}{\mu} (-\nabla P + \rho \mathbf{g}) \quad (1)$$

where  $P$  is the pressure,  $\rho$  is the density of water and  $\mathbf{g}$  is the gravity field, pointing in the  $z$  direction. Note the the volume flux  $\mathbf{U}$  is related to the fluid velocity  $\mathbf{U}_f$  by the porosity  $\varphi$  of the matrix such that  $\mathbf{U} = \varphi \mathbf{U}_f$ . In addition to Darcy’s law, the flow is assumed to be incompressible, so that the volume flux must also satisfy a continuity equation,

$$\partial_x U + \partial_z W = 0. \quad (2)$$

Water motion inside the core is driven by buoyancy and temperature differences. We model the effects of temperature on density assuming linear expansion of the fluid

with temperature under the Boussinesq approximation, such that  $\rho = \rho_0(1 - \alpha(T - T_0))$  where  $\rho_0$  is a reference density and  $\alpha$  the thermal expansion coefficient. Darcy's law may thus be written as,

$$\mathbf{U} = \frac{k}{\mu} (-\nabla P' + \rho_0 g \alpha \Theta \mathbf{e}_z) \quad (3)$$

where  $P' = P + \rho_0 g z$  and  $\Theta \equiv T - T_0$ . Since the flow is driven by thermal anomalies  $\Theta$ , we must introduce an equation modelling the transport of heat inside the porous medium. This is achieved using thermal energy conservation, in which a source term accounting for volume heat production is included (Nield & Bejan, 2013; Souček et al., 2014):

$$\bar{\varphi} \partial_t \Theta + \mathbf{U} \cdot \nabla \Theta = \kappa \nabla^2 \Theta + q \quad (4)$$

with  $\kappa$  the volume-averaged heat diffusivity inside the porous medium (*i.e.* of both water and the porous matrix together),  $\bar{\varphi}$  a modified porosity and  $q$  is the internal heat source term. Under the assumption of local thermal equilibrium between the fluid and the matrix, the modified porosity  $\bar{\varphi}$  and the volume-averaged diffusivity are combinations of the porosity,  $\varphi$ , the heat capacity per unit of mass of the matrix and water,  $c_m$  and  $c_0$ , and the density of the matrix and water,  $\rho_m$  and  $\rho_c$ , such that

$$\bar{\varphi} = \frac{(1 - \varphi)\rho_m c_m + \varphi \rho_0 c_0}{\rho_0 c_0} \quad \text{and} \quad \kappa = \frac{(1 - \varphi)\lambda_m + \varphi \lambda_0}{\rho_0 c_0}, \quad (5)$$

133 (Nield & Bejan, 2013; Souček et al., 2014), where the  $\lambda_{m,0}$  are the heat conductivity of  
 134 the matrix and water. The source term  $q$  is related to the volumetric heat production  
 135 by tidal heating  $Q_V$  via  $q = Q_V/(\rho_0 c_0)$ . In this paper, we consider two idealised lim-  
 136 its: either  $Q_V$  is constant or it is assumed to vary laterally (*i.e.* in  $x$ ) to model tidal heat-  
 137 ing inhomogeneities.

## 138 2.2 Boundary conditions

Throughout this work, we impose periodic boundary conditions in the horizontal direction. The bottom of the porous layer roughly corresponds to the core centre, and so we assume that there is no heat or mass flux crossing the bottom boundary, that is:

$$\partial_z \Theta(z = 0) = 0 \quad \text{and} \quad W(z = 0) = 0 \quad (6)$$

The top of the layer at  $z = h$  is in contact with the ocean and must allow mass exchange between the core and the ocean. This is achieved by imposing a purely vertical velocity at the top, *i.e.* :

$$U(z = h) = 0. \quad (7)$$

The two layers are also thermally coupled, and we consider two possible boundary conditions for  $\theta$  on the upper boundary. One first natural choice is to impose the temperature (on the upper boundary) to be the temperature of the ocean, *i.e.* ,

$$\Theta(z = h) = 0 \quad (8)$$

However, in this case, the advective heat flux driving hydrothermal activity  $W\Theta(z = h)$  across the interface would vanish, which seems at odds with the idea that the water coming out the porous layer may drive a buoyant plume rising in the ocean. We could alternatively use another boundary condition where the temperature of water is left unchanged as it leaves the porous layer, while water enters with the imposed temperature of the ocean, that is,

$$\begin{cases} \partial_z \Theta(z = h) = 1 & \text{if } W > 0 \\ \Theta(z = h) = 0 & \text{else.} \end{cases} \quad (9)$$

139 Such a boundary condition is a standard parametrisation of core–ocean interactions (Rabinowicz  
 140 et al., 1998; Monnereau & Dubuffet, 2002; Cserepes & Lenkey, 2004; Choblet et al., 2017).

141 The thermal boundary conditions (8) and (9) may be regarded as two end-members  
 142 of the fully coupled problem of the core–ocean interaction. In the case of slow ascent in  
 143 the porous medium, diffusion from the ocean inside the core causes the temperature inside  
 144 the porous medium to drop in the top boundary vicinity. Conversely, if the upwelling  
 145 is fast, diffusion is not able to affect the temperature inside the ascending plume. As a  
 146 side note, intermediary situations where  $\partial_z \Theta(z = h) = -\beta$  with  $\beta > 0$  could also be  
 147 considered. Nevertheless, choosing between the two boundary conditions or parametri-  
 148 sation of  $\beta$  would require a demanding study of the fully coupled system involving both  
 149 the ocean and the porous core. We instead carry out two sets of simulations using ei-  
 150 ther boundary conditions (8) and (9). We will find that the choice of boundary condi-  
 151 tion does not significantly affect the flow in the interior of the core.

### 152 2.3 Scaling the problem: dimensionless equations

First, all considered lengths are normalised by the height of the porous layer  $h$ . We  
 must also define volume flux and temperature scales, respectively denoted as  $U^*$  and  $\Theta^*$ .  
 Darcy’s law (3) gives a simple relation between these two scales,

$$U^* = \frac{k}{\mu} \rho_0 \alpha g \Theta^* . \quad (10)$$

Unlike in, say, Rayleigh–Bénard set-up, the temperature scale  $\Theta^*$  is not naturally im-  
 posed in the internally heated problem. We predict that in the non-linear regime, heat  
 production and advection will be the dominant balance in (4), leading to the following  
 relation between the velocity and temperature scales,

$$U^* \Theta^* = h q . \quad (11)$$

Both scales then can be written as a function of physical parameters as follows:

$$U^{*2} = \frac{k}{\mu} \rho_0 \alpha g h q \quad \text{and} \quad \Theta^* = \sqrt{\frac{\mu h q}{k \rho_0 \alpha g}} \quad (12)$$

Given these scales, we find that the system is governed by only one dimensionless pa-  
 rameter, a Rayleigh number comparing the relative importance of advection and diffu-  
 sion,

$$Ra \equiv \frac{h U^*}{\kappa} = \left( \frac{k \alpha g}{\kappa \nu} \frac{q h^2}{\kappa} h \right)^{1/2} . \quad (13)$$

153 Note that other definitions have been considered for the Rayleigh number, depending  
 154 in particular on the expected balance at play. For instance, Burretta and Berman (1976)  
 155 choose volume flux and temperature scales based on an advection and diffusion balance,  
 156 rather than a balance between advection and heat production consider in (11), leading  
 157 to a Rayleigh number  $Ra_{bb} = Ra^2$ .

Introducing the dimensionless temperature  $\theta = \Theta/\Theta^*$ , volume flux  $\mathbf{u} = \mathbf{U}/U^*$ ,  
 the dimensionless governing equations for a porous layer with internal heating are:

$$\left\{ \begin{array}{l} \nabla \cdot \mathbf{u} = 0 \\ \mathbf{u} = -\nabla p + \theta \mathbf{e}_z \\ \partial_t \theta + \mathbf{u} \cdot \nabla \theta = \frac{1}{Ra} \nabla^2 \theta + 1 \end{array} \right. \quad (14)$$

where time is normalised by  $\bar{\varphi} h/U^*$  and pressure is rescaled by  $\mu U^*/(hk)$ . The flow be-  
 ing incompressible and two-dimensional, it is convenient to introduce a stream function  
 $\psi$  such that  $\mathbf{u} = \nabla \times (-\psi \mathbf{e}_y)$ . The governing equations (14) become

$$\left\{ \begin{array}{l} \nabla^2 \psi = -\partial_x \theta \\ \partial_t \theta + \partial_z \psi \partial_x \theta - \partial_x \psi \partial_z \theta = \frac{1}{Ra} \nabla^2 \theta + 1. \end{array} \right. \quad (15)$$

Lastly the vertical boundary conditions are

$$w(z = 0) = u(z = 1) = \partial_z \theta(z = 0) = 0, \quad (16)$$

and either

$$\text{BC 1: } \theta(z = 1) = 0, \quad \text{or} \quad (17)$$

$$\text{BC 2: } \begin{cases} \partial_z \theta(z = 1) = 1 & \text{if } w > 0, \\ \theta(z = 1) = 0 & \text{else,} \end{cases} \quad (18)$$

158 for the temperature. Note that the boundary conditions on the volume flux translate into  
159  $\partial_z \psi(z = 1) = \psi(z = 0) = 0$ . Lastly, the domain is periodic in the  $x$  direction.

## 160 2.4 Numerical modelling

161 We study this problem numerically with the code developed by (Hewitt et al., 2012).  
162 At each time step, Darcy's law is used to determine the stream function using Fourier  
163 transform in the horizontal direction and second order finite differences in the vertical  
164 direction. The time evolution of the advection-diffusion equation is solved using an al-  
165 ternating direction implicit scheme (Press et al., 1992). The diffusion term is discretised  
166 using standard second-order accurate finite differences and the use of two staggered grids  
167 for the stream function  $\psi$  and the temperature field  $\theta$  allows flux-conservative discreti-  
168 sation of the advection term. The finite difference in time is second-order accurate as  
169 well. Anticipating strong gradients near the boundaries, a vertical stretched grid is im-  
170 plemented to ensure the boundary layers are well resolved. The numerical discretisation  
171 of equations (15) is tested in section 3.

## 172 3 The onset of convection

In this section, we investigate both theoretically and numerically the critical value  
of the Rayleigh number  $Ra$  above which a convective instability develops. The steady,  
purely diffusive base ( $\mathbf{u} = 0, \theta_b$ ) state on which the instability develops is

$$\theta_b(z) = \frac{Ra}{2} (1 - z^2) \quad (19)$$

regardless of the upper thermal boundary condition. We look for perturbations to the  
base state of the form (Drazin, 2002) :

$$\psi = \psi_1(\mathbf{x})e^{\sigma t} \quad \text{and} \quad \theta = \theta_b + \theta_1(\mathbf{x})e^{\sigma t} \quad (20)$$

such that  $|\psi_1|, |\theta_1| \ll \theta_b$ . The exponential terms allow to account for the existence of  
convective instability characterised by  $\text{Re}(\sigma) > 0$ . Using the ansatz (20), equations (15)  
to leading order in  $\psi_1, \theta_1$  yield the following single, fourth-order differential equation on  
the stream function:

$$\nabla^4 \psi_1 = Ra\sigma \nabla^2 \psi_1 - zRa^2 \partial_{xx} \psi_1. \quad (21)$$

The invariance under translation along the  $x$ -axis allows further simplification by assum-  
ing that  $\psi_1$  is a plane wave in  $x$ , that is  $\psi_1 = \hat{\psi}_1(z) \exp(ikx)$ . Equation (21) with the  
plane wave assumption yields the following ordinary differential equation for the func-  
tion  $\hat{\psi}_1$ :

$$\hat{\psi}_1'''' - (2k^2 + Ra\sigma)\hat{\psi}_1'' + (k^4 + Ra\sigma k^2 - zRa^2 k^2)\hat{\psi}_1 = 0 \quad (22)$$

173 where  $\sigma$  is an unknown eigenvalue. We solve numerically the one-dimensional bound-  
174 ary value problem (22) using BC 1 in (17). (In fact, for this onset problem, BC 2 (18)  
175 gives an ill-posed system.) We find the lowest value of the Rayleigh number for which  
176  $\sigma = 0$  to be  $Ra = Ra_c \simeq 5.894$  at  $k = k_c \simeq 1.751$ . Such a value for the critical  
177 Rayleigh number is close to the value 5.72 found experimentally and theoretical by Buretta

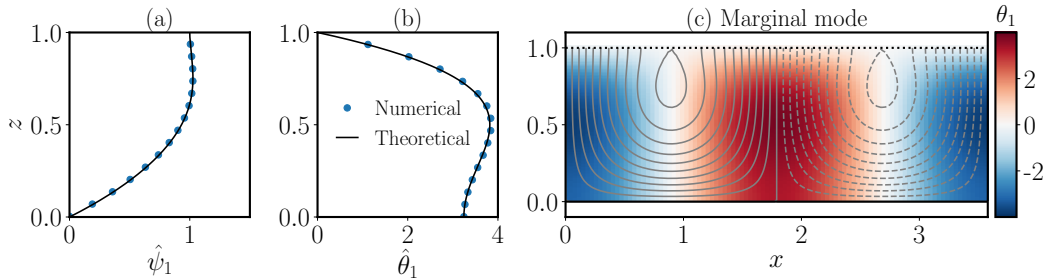


**Figure 2.** (a) and (b): Vertical structure functions of the stream function  $\hat{\psi}_1$  and  $\hat{\theta}_1$  of the marginal mode obtained by solving the boundary value problem (22) (black line) and extracted from a direct numerical simulation of the instability close to the threshold ( $Ra - Ra_c \simeq 3 \times 10^{-2}$ ). (c) Temperature field ( $\theta_1$ ) and streamlines (iso-contours of  $\psi_1$ ) of the unstable mode at the onset of convection.

178 and Berman (1976) in a system with closed boundary conditions. The marginal mode  
 179 and its vertical structure functions ( $\hat{\psi}_1$  and  $\hat{\theta}_1$ ) are shown in figure 2. The mode com-  
 180 prises a half-roll structure, with strong horizontal flow at the lower boundary and strong  
 181 vertical flow at the upper boundary. The temperature deviation is maximised roughly  
 182 half-way up the roll.

183 We use this theoretical investigation of the onset of convection to benchmark the  
 184 numerical code. Simulations were carried out at values of the Rayleigh number  $Ra$  very  
 185 close to the onset ( $|Ra - Ra_c| \leq 10^{-1}$  typically). The horizontal extent of the domain  
 186 is chosen to match approximately twice the wave length of the marginal mode. Comput-  
 187 ations were initiated with a small perturbation to the diffusive temperature profile (19).  
 188 We observed an exponential growth or decay of the amplitude of the perturbation to the  
 189 diffusive base state and found accurate reproduction of both the critical Rayleigh num-  
 190 ber and the growth or decay rate of the most unstable mode for nearby values of  $Ra$ .  
 191 Figure 2 shows the excellent agreement between the theoretical and the computed verti-  
 192 cal structure functions  $\hat{\theta}_1$  and  $\hat{\psi}_1$ .

## 193 4 Non-linear heat transport by convection

194 In the following section, we investigate heat transport by convection for larger val-  
 195 ues of  $Ra$ . We first describe qualitatively the organisation of the flow as  $Ra$  is increased.  
 196 We then show quantitatively that non-linear heat transport is dominated by advection,  
 197 which constrains the typical size of hot plumes and thermal anomalies. We use both ther-  
 198 mal boundary conditions (17) and (18) to find that the difference between them is neg-  
 199 ligible for large enough values of  $Ra$ .

### 200 4.1 Numerical process

201 Prior to delving into the results of the simulations, we explain how a typical num-  
 202 erical simulation is carried out. The simulations are initialised with random noise at  
 203 a certain Rayleigh number  $Ra$ . After the initial growth of the instability, the flow reaches  
 204 a statistically steady state. It is assessed by computing at each time step the mean of  
 205 the maximum temperature since the start of the simulation: such a cumulative average  
 206 converges towards a constant once the statistically steady state is reached. The simu-  
 207 lation is terminated once the steady state has lasted for 300 time units. The Rayleigh  
 208 number is then switched to a new value, and the simulations is initiated with the last

Boundary conditions	Aspect ratio $L$	Rayleigh number range	Resolution ( $n_x \times n_z$ )
BC 1, 2	4	6-20	$128 \times 300$
		20-100	$256 \times 300$
		100-770	$512 \times 400$
		550-2000	$1024 \times 500$
		3000-10000	$2048 \times 500$
BC 2	3	6-20	$128 \times 300$
		20-100	$256 \times 300$
		100-770	$512 \times 400$
		550-2000	$1024 \times 500$
		3000-10000	$2048 \times 500$
BC 2	8	6-20	$256 \times 300$
		20-100	$512 \times 300$
		100-770	$1024 \times 400$
		550-3000	$2048 \times 500$

**Table 1.** Table of all the numerical simulations carried out indicating the nature of the boundary condition, the aspect ratio of the domain, the range of Rayleigh numbers and the associated horizontal ( $n_x$ ) and vertical ( $n_z$ ) resolutions. Note that the resolution is increased close to the boundaries by the use of a stretched vertical grid.

209 state of the previous one plus a small noise disturbance. A summary of all the numer-  
210 ical simulations that have been carried out is given in table 1.

## 211 4.2 Flow structures and organisation

212 To introduce the non-linear behaviour of the instability driven by internal heat-  
213 ing, we first to illustrate typical flow patterns observed at different Rayleigh numbers.  
214 Figures 3 displays typical snapshots of the temperature field. At low Rayleigh number,  
215 *i.e.* for  $Ra_c \leq Ra < 20$ , the convection reaches a steady state with few plumes, be it  
216 for boundary condition BC 1 or BC 2 (see figure 3a). Similar to the unstable mode at  
217 threshold, these plumes consist of half-rolls, although with steeper vertical gradients at  
218 the top boundary in the case of BC 1. For larger Rayleigh numbers (see 3b), the flow  
219 exhibits an unsteady chaotic behaviour where usually two modes with different number  
220 of plumes alternate, thus inducing chaotic merging and growth of plumes. This situa-  
221 tion ceases for  $Ra \simeq 600$ , at least for an aspect ratio  $L = 4$ : higher values of the Rayleigh  
222 number give rise to steady solutions with a large number of narrow plumes (see figure  
223 3c)

224 The only noticeable difference between the two boundary conditions is the existence  
225 of a thin thermal boundary layer when the top temperature is imposed (BC 1). Its thick-  
226 ness, of order  $Ra^{-1}$ , is set by a balance between vertical advection and diffusion. In ad-  
227 dition, the high degree of similarity between the simulations carried out with different  
228 boundary condition suggests that the mixed boundary condition (BC 2) is reliable. Note  
229 that this is not the case below the threshold of the instability where flows that are highly  
230 sensitive to initial condition are observed. We therefore choose to use both boundary con-  
231 ditions in the study detailed hereafter, as long as  $Ra > Ra_c$ . Lastly, note that in these  
232 snapshots  $\theta = \mathcal{O}(1)$ , which confirms that the balance between advection and heat pro-  
233 duction drives the dynamics, a balance that was foreseen in section 2.3.

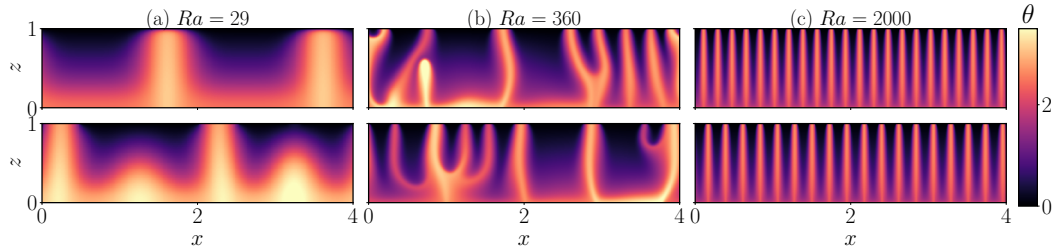


**Figure 3.** Snapshots of the temperature field  $\theta$  at  $Ra = 29, 360$  and  $2000$  for boundary condition BC 1 (**top**) and BC 2 (**bottom**), taken once a statistically steady state is reached. The flow exhibits chaotic behaviour for the two lowest values of the Rayleigh number, and is steady at  $Ra = 2000$ . Apart from the thin top boundary layer, both boundary conditions (17) and (18) overall produce the same flow. The difference in the plume number at  $Ra = 2000$  between the two boundary conditions is rather due to the simultaneous stability of different modes.

234

### 4.3 Advective heat transport

235

236

237

238

239

240

The qualitative analysis of snapshots carried out in the preceding section indicates that advection dominates heat transport. We propose in the following a quantitative analysis of the flow to support this assertion, in particular of the vertical temperature and heat flux profiles. This analysis will allow us to compare internally heated porous convection with the more classical Rayleigh-Bénard problem via the introduction of a generalised Nusselt number.

241

#### 4.3.1 The mean temperature scale

242

243

244

245

246

247

248

249

250

251

252

253

254

255

256

257

258

259

260

261

It has been noted in the preceding section that the typical values of the temperature field remain of  $O(1)$ . To better quantify this observation, we introduce a dimensionless temperature scale  $\Delta\theta = \bar{\theta}(z=1) - \bar{\theta}(z=0)$ , where the operation  $\bar{\cdot}$  denotes horizontal and temporal average in the statistically steady state. Typical profiles of the horizontally averaged temperature are shown in figure 4a. The average temperature is a decreasing function of height that converges towards an asymptotic profile at high Rayleigh number. We note again the strong similarity between the two boundary conditions, especially at large Rayleigh numbers where they only differ by the presence of the top thermal boundary layer. The temperature scale  $\Delta\theta$  is also plotted in figure 4 as a function of the Rayleigh number for all simulations. We note it is well below the diffusive scaling  $\Delta\theta \propto Ra$  even very close to the threshold of the instability.  $\Delta\theta = O(1)$  is a signature of efficient transport and vertically mixing of the thermal energy by the convective flows. In addition, we note a marked decrease of  $\Delta\theta$  at  $Ra \simeq 600$ , which corresponds to the transition from the chaotic to the steady regime. It indicates that the steady flow is even more efficient at transporting heat out of the system. Anomalous points may however be noticed; they are due to the locking of the simulation on a particular mode (*i.e.* a flow with a certain number of plumes) that remains stable as the Rayleigh number is slightly increased. We found that starting from a different initial condition at the same Rayleigh number can give steady states with a different number of plumes, which suggests that the past history of the system has some influence on its current state.

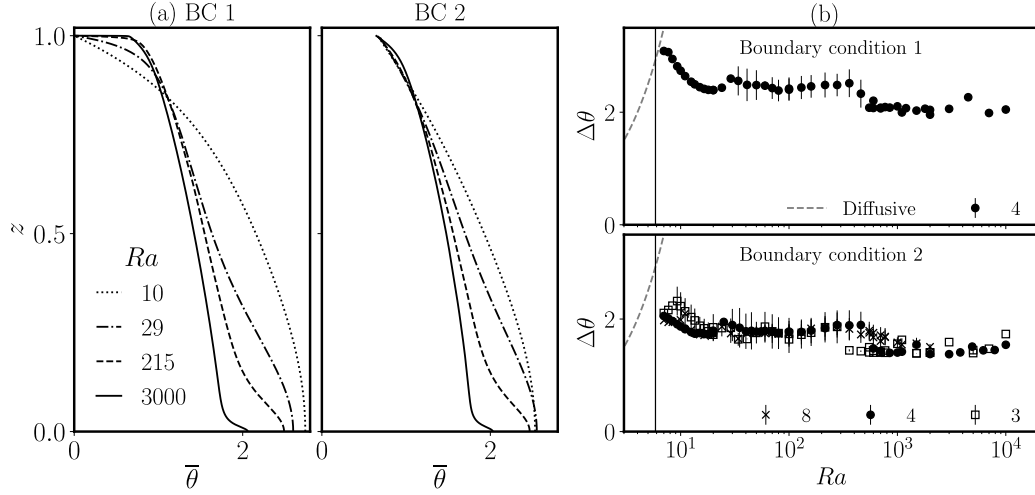


**Figure 4.** (a) Averaged temperature profiles  $\bar{\theta}(z)$  for different Rayleigh numbers and both boundary conditions and aspect ratio  $L = 4$ . At large  $Ra$ , the profiles given by BC 1 and BC 2 are strikingly similar apart from the upper boundary layer for BC 1. Note the emergence of a thermal boundary layer at  $z = 0$  where the heat that is produced locally is carried away through diffusion only. Although it creates sharp variations, the bottom boundary condition  $\bar{\theta}'(0) = 0$  remains satisfied even when rapid variations are observed at  $Ra = 3000$ . (b) Mean temperature difference between the bottom and the top of the porous layer  $\Theta^*$  as a function of the Rayleigh number  $Ra$ , for all simulations carried out with BC 1 (top) and BC 2 (bottom). The errorbars correspond to the standard deviation over time of the average temperature difference. The diffusive temperature difference  $\Delta\theta = Ra/2$  is shown for comparison (dashed line). The vertical line marks the critical Rayleigh number  $Ra_c$ .

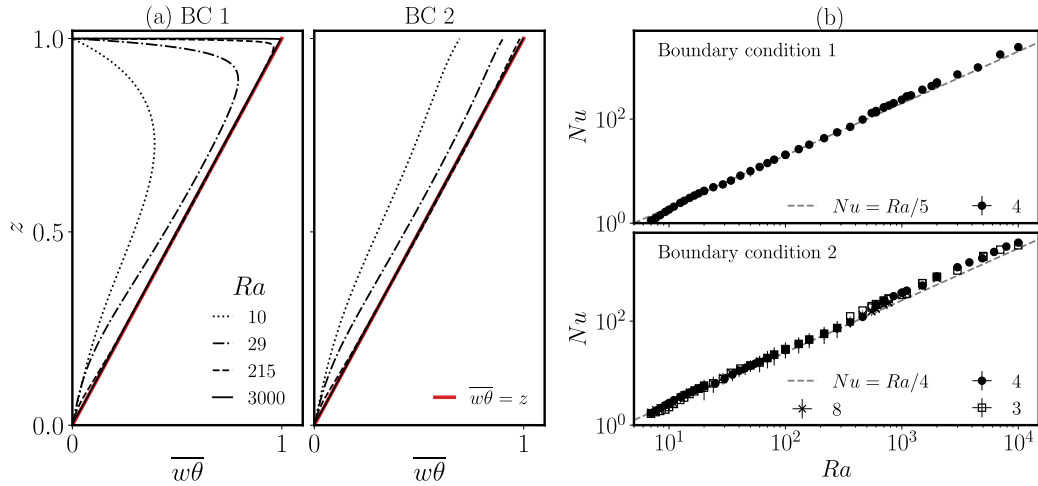


**Figure 5.** (a) Vertical variations of the horizontally-averaged advective heat flux  $\overline{w\theta}(z)$ , for boundary condition BC 1 (left) and 2 (right) and aspect ratio  $L = 4$ . Again, we note the similarity between the two boundary condition in the bulk of the porous medium. The asymptotic law  $\overline{w\theta} = z$  (25) is given for reference. (b) Plot of the Nusselt number  $Nu$  as a function of the Rayleigh number  $Ra$  for all simulations carried out with boundary conditions BC 1 & 2 (top and bottom panels respectively). The errorbars correspond to the standard deviation in time of the instantaneous Nusselt number  $N(t)$  (see equation (26)).

262

### 4.3.2 The advective flux

To further quantify heat transport in the strongly non-linear regime, we consider here the vertical heat flux, defined as

$$J = w\theta - \frac{1}{Ra} \frac{\partial \theta}{\partial z}, \quad (23)$$

which comprises an advective and a diffusive contribution. Time-averaged thermal energy conservation (14) prescribes a balance between vertical heat transport and volumetric heat production such that:

$$\frac{d\bar{J}}{dz} = 1, \quad \text{that is } \bar{J}(z) = z. \quad (24)$$

In the asymptotic regime of high Rayleigh number, we expect that the heat produced is carried away by advection only, apart from the thermal boundary layer when it exists. In the bulk of the porous medium, we thus expect

$$\overline{w\theta}(z) = z. \quad (25)$$

263

264

265

266

267

As can be noticed in figure 5, the advective heat flux is well described by the asymptotic law (25) even at Rayleigh numbers as low as  $Ra = 29$ . For BC 1, this agreement breaks down near the upper boundary where  $\theta = 0$ : the advection flux in the bulk is converted into a conductive heat flux over a boundary layer of depth  $\mathcal{O}(Ra^{-1})$  which follows from equation (23).

268

### 4.3.3 Nusselt number

It is interesting to assess how efficient the convecting system is at transporting heat relative to purely diffusive transport. It is quantified by a Nusselt number  $N$  that provides a comparison between the total heat flux (including advective and diffusive contributions) and the diffusive heat flux (see *e.g.* Goluskin (2016)),

$$N(t) \equiv \frac{\langle w\theta - Ra^{-1}\partial_z\theta \rangle}{-Ra^{-1}\langle \partial_z\theta \rangle} = \frac{Ra}{2\Delta\theta}, \quad (26)$$

269

270

271

272

273

274

275

276

277

278

$\langle \cdot \rangle$  denoting volume average, and where we have used that  $\langle w\theta - Ra^{-1}\partial_z\theta \rangle = \langle z \rangle = 1/2$  and  $\langle \partial_z\theta \rangle = \Delta\theta$  from (23) and (24). Then, we define the mean Nusselt number  $Nu$  to be the long-time average of  $N(t)$ . Note that we retrieve that the transport is purely diffusive at threshold, since, at  $Ra = Ra_c$ ,  $\Delta\theta = Ra/2$  so that  $Nu = 1$ . Because  $\Delta\theta = \mathcal{O}(1)$ , we predict that, in the high Rayleigh number regime,  $Nu \propto Ra$ . For both boundary conditions BC 1 & 2, our simulations confirm this scaling down to  $Ra \sim 20$  (see figure 5b). There is a slight enhancement of the efficiency of heat transport as steady states emerge in the non-linear regime of the instability around  $Ra \sim 500$ . The same scaling between  $Nu$  and  $Ra$  is also found in the classical Rayleigh-Bénard set-up in a porous medium (Otero et al., 2004; Hewitt et al., 2012, 2014).

279

## 4.4 Plume scales

In section 4.2, we observed that as the Rayleigh number  $Ra$  is increased, the typical width of the plumes and their typical spacing decreases. We obtain a quantitative measure of the mean plume size  $\ell_p$  and separation  $\Delta x_p$  as a function of the Rayleigh number from the heat flux at the upper boundary. As shown in figure 6a, plumes produce a series of heat-flux peaks. At each time step, we record the mean plume width  $\hat{\ell}_p$  and plume separation distance  $\hat{\Delta x}_p(t)$  over all plumes, and we define  $\ell_p$  and  $\Delta x_p$  to be their long-time averages. Typical variability is given by the standard deviation of  $\hat{\ell}_p$  and  $\hat{\Delta x}_p$  over time. The result of this process is shown in figure 6(b,c): both the plume width and separation exhibit the same scaling with the Rayleigh number, that is  $\ell_p, \Delta x_p \propto Ra^{-1/2}$ ,

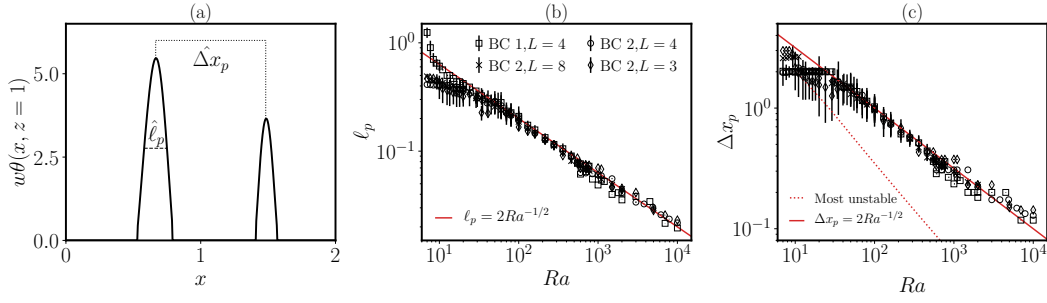


**Figure 6.** (a) vertical advective heat flux at the top boundary for  $Ra = 200$  with boundary condition BC 2 and aspect ratio  $L = 4$ . The plot focuses on two plumes and shows graphically the definition of the plume separation  $\hat{\Delta}x_p$  and the plume width  $\hat{\ell}_p$ . (b, c) mean plume size  $\ell_p$  and plume separation  $\Delta x_p$ , respectively, for all simulations with both boundary conditions BC 1 and BC 2. Both quantities scale with the Rayleigh number as  $Ra^{-1/2}$ . The errorbars are determined by the standard deviation of the mean plume width and separation over a numerical run. The red dashed line indicates the plume separation for the most unstable mode, which follows a  $Ra^{-3/4}$  power law.

even close to the threshold. This power law can't be explained by linear theory, even at low  $Ra$ , as the mean separation between plumes does not coincide with the most unstable mode predicted by the linear stability analysis (see figure 6c). Instead, the typical scale of the plume is controlled by a balance between vertical advection, horizontal diffusion and heat production in (14), that is,

$$w\partial_z\theta \sim Ra^{-1}\partial_{xx}\theta \sim 1. \quad (27)$$

280 Given that temperature contrast remains  $O(1)$ , this balance demands both that the ver-  
 281 tical velocity of the plume is  $O(1)$  and that the typical lateral scale of the plume must  
 282 be proportional to  $Ra^{-1/2}$ .

#### 283 4.5 Asymptotic plume solution

284 Building on the scalings governing the typical plume size found numerically and  
 285 theoretically, we derive here fully non-linear solutions of the equations (14) in the asymp-  
 286 totic limit  $Ra \rightarrow \infty$ . As explained below, the derivation of these equations allows us  
 287 to understand the balance at play in the plume formation.

In the bulk of the porous medium, since the gradients are  $O(Ra^{1/2})$  in the  $x$  di-  
 rection and  $O(1)$  in the  $z$  direction, the incompressibility condition  $\partial_x u + \partial_z w$  imposes  
 a scaling on the ratio between  $u$  and  $w$ , that is  $u/w = O(Ra^{-1/2})$ . We thus introduce  
 the rescaled variables  $\hat{x}$  and  $\hat{u}$  such that:

$$x = Ra^{1/2}\hat{x} \quad \text{and} \quad u = Ra^{-1/2}\hat{u}. \quad (28)$$

With these rescaled variables, the incompressibility condition is

$$\partial_{\hat{x}}\hat{u} + \partial_z w = 0 \quad (29)$$

Taking the curl of Darcy's law in (14) yields

$$\partial_{\hat{x}}w = \partial_{\hat{x}}\theta + O(Ra^{-1}). \quad (30)$$

Hence, to leading order in  $Ra$ ,  $\theta - w$  is a function of  $z$  only. Because  $\bar{w} = 0$ , we infer  
 that  $\theta(\hat{x}, z) = w(\hat{x}, z) + \bar{\theta}(z)$ . Thus, Darcy's law compels the temperature and the

vertical velocity to have the same horizontal variance. Lastly, the advection-diffusion equation in (14) with rescaled variables is

$$\partial_t \theta + \hat{u} \partial_{\hat{x}} \theta + w \partial_z \theta = \partial_{\hat{x}\hat{x}} \theta + 1 . \quad (31)$$

288

where all terms appear to be of the same order.

Building on our numerical results, we seek steady solutions that are periodic in the  $x$  direction. We introduce an ansatz for the flow that is the lowest order truncation of a Fourier series, that is, we assume the velocity field to have the following form,

$$\begin{cases} \hat{u} &= \hat{u}_0(z) \sin(\hat{k}\hat{x}) \\ w &= w_0(z) \cos(\hat{k}\hat{x}) , \end{cases} \quad (32)$$

which has no mean mass flux in either vertical or horizontal direction. According to the rescaled Darcy's law (30), the temperature becomes

$$\theta = w + \bar{\theta}(z) = w_0(z) \cos(\hat{k}\hat{x}) + \bar{\theta}(z) . \quad (33)$$

For the flow (32) to satisfy the incompressibility condition, the following relation is required:

$$w'_0 = -\hat{k} \hat{u}_0 . \quad (34)$$

To determine the functions  $w_0$  and  $\bar{\theta}$ , we use the advection-diffusion equation (31) which becomes

$$w_0 w'_0 \frac{1 - \cos(2\hat{k}\hat{x})}{2} + w_0 w'_0 \frac{1 + \cos(2\hat{k}\hat{x})}{2} + w_0 \bar{\theta}' \cos(\hat{k}\hat{x}) = -\hat{k}^2 w_0 \cos(\hat{k}\hat{x}) + 1 \quad (35)$$

where the incompressibility condition (34) and Darcy's law (30) have been used. This equation contains mean and  $\hat{k}$  harmonic terms that must be balanced, respectively. The mean terms simply yields a balance between vertical heat advection and heat production, that is:

$$\frac{dw_0^2}{dz} = 2 \quad i.e. \quad w_0 = \sqrt{2z} . \quad (36)$$

The harmonic  $\hat{k}$  terms correspond to a balance between horizontal diffusion and the vertical advection of the average thermal energy (or temperature) profile,

$$w_0 \bar{\theta}' = -\hat{k}^2 w_0 \quad i.e. \quad \bar{\theta}(z) = \theta_0 - \hat{k}^2 z . \quad (37)$$

289

As noted in the preceding section, such a balance is responsible for setting the  $O(Ra^{1/2})$  horizontal gradients.

290

We have, therefore, constructed a fully non-linear solution that is exact in the asymptotic limit  $Ra \rightarrow \infty$ , and is given by

$$\begin{cases} u &= -\frac{Ra^{-1/2}}{\hat{k}\sqrt{2z}} \sin(Ra^{1/2}\hat{k}x) \\ w &= \sqrt{2z} \cos(Ra^{1/2}\hat{k}x) \\ \theta &= \theta_0 - \hat{k}^2 z + \sqrt{2z} \cos(Ra^{1/2}\hat{k}x) \end{cases} \quad (38)$$

291

where  $\hat{k}$  and  $\theta_0$  are  $O(1)$  but *a priori* unknown. Note that this solution only satisfies one boundary condition: the absence of mass flux at the bottom of the porous layer. The remaining boundary conditions, be it the absence of bottom heat flux, the purely vertical velocity at the top, or either of the thermal boundary condition BC 1 or BC 2, are all unmatched with the solution.

292

293

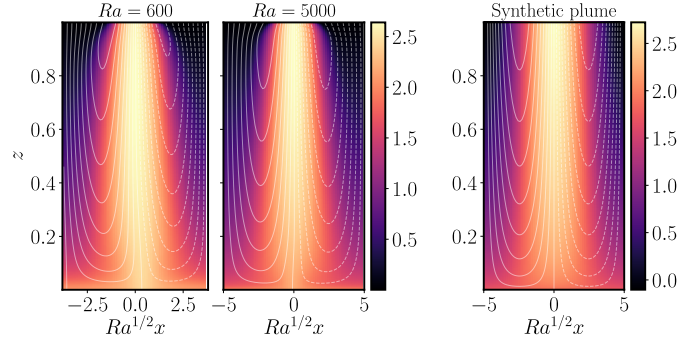
294

295

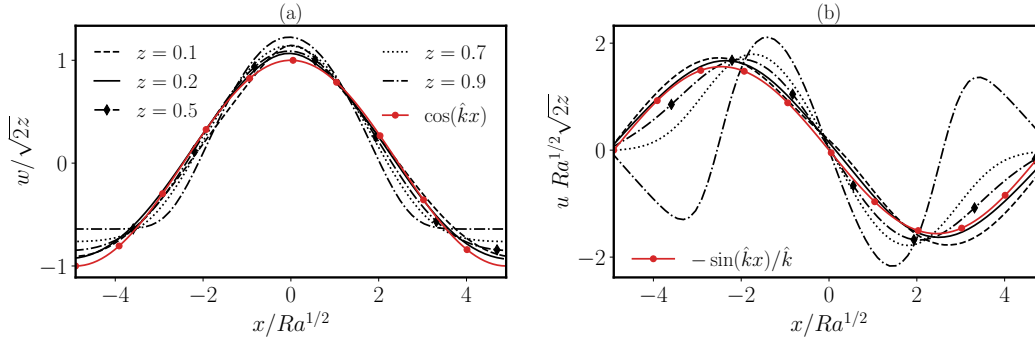
296

Figure 7 provides a comparison between plumes extracted from the simulations at two different Rayleigh numbers with a synthetic plume corresponding to the solution (38).

297



**Figure 7.** **Left:** single plume isolated in the regime where the flow is steady and periodic in  $x$ , with boundary condition BC 1. **Right:** synthetic field for a single plume obtained from the solution (38). The rescaled wave number  $\hat{k}$  is chosen to match the  $Ra = 5000$  case, and its value is around 0.64. The integration constant  $\theta_0$  is chosen around 1.8 to roughly match the bottom temperature profiles observed in 4. Note that although the streamlines do not seem to be vertical at the top boundary, a zoom shows that they ultimately bend to match verticality very close to the top boundary.



**Figure 8.** Horizontal profiles at different heights  $z$  of the scaled vertical **(a)** and horizontal **(b)** velocity across a plume. The amplitudes are normalised accordingly to the non-linear solution (38). The expected structure is shown in red and the only fitting parameter is the rescaled wave number  $\hat{k} \simeq 0.64$ . The Rayleigh number is  $Ra = 5000$  and the top boundary condition is BC 2.

298  
299  
300

The overall qualitative behaviour of the two fields are the same, although the theoretical solution does not capture the shrinking of the plumes close to the top boundary, because it does not satisfy the boundary condition there.

301  
302  
303  
304  
305  
306  
307  
308

To draw a more quantitative comparison between the non-linear solution and the flow in one plume, we plot in figure 8 several horizontal cuts at different heights of the vertical and horizontal velocities. We find that in the bulk, the theoretical solution adequately describes the amplitude of the velocity variations. However, the model becomes inaccurate near the upper boundary where, as noted above, it does not satisfy the correct boundary conditions. In fact, this issue seems to lead to other inaccuracies in the model: it predicts a linear decrease in the mean temperature  $\bar{\theta}$ , whereas the numerical simulations show a more complex dependence on  $z$  (figure 4).

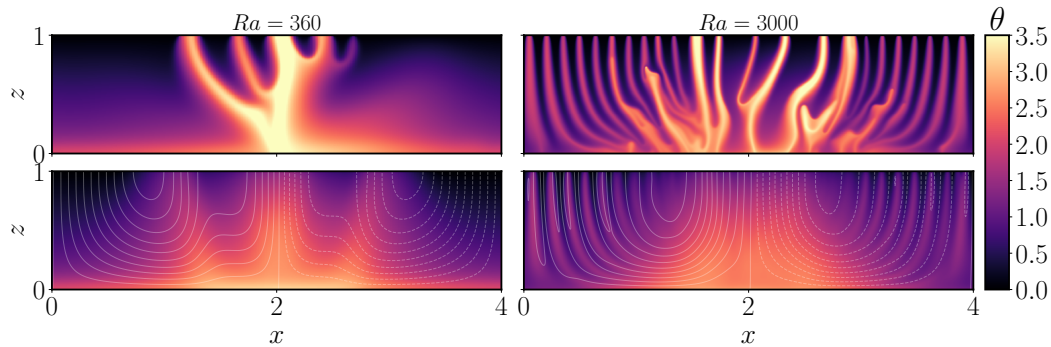


**Figure 9.** Snapshot of the temperature field for the heterogeneous heating case (**top**) and the time-averaged temperature and flow streamlines averaged (**bottom**).

309

#### 4.6 Conclusion for non-linear heat transport

310

311

312

313

314

315

316

317

318

319

320

321

322

323

Throughout this section, we have detailed the properties of heat transport by convection in strongly non-linear regimes. Based on several arguments, including temperature scale, heat flux and Nusselt number measurement, we have confirmed that heat transport is dominated by advection in the bulk of the porous medium. We have carried out simulations with two different top boundary conditions that are thought to be relevant to geophysical context: one where the top boundary temperature is imposed, and another where advective heat flux is conserved in upwellings and temperature is imposed in downwellings. We have confirmed that the two boundary conditions produce the same bulk flows. Lastly, we have shown that the typical plume size follows a  $Ra^{-1/2}$  power law, which is due to a balance between horizontal diffusion and vertical advection of heat. It is interesting to note that internally-heated and Rayleigh-Bénard convection are different regarding the typical plume scale: in the asymptotic regimes of large  $Ra$ , Hewitt et al. (2012) found that  $\ell_p$  scaled like  $Ra^{-0.4}$ , which they later suggested was a result of the stability of the plumes (Hewitt & Lister, 2017).

324

## 5 Accounting for the large scale modulation of tidal heating

325

### 5.1 A simple model

In this section, we briefly explore how the large-scale variations of tidal heating affect heat transport in internally heated porous media. This is important for the case of icy satellites such as Enceladus, for which heterogeneity of tidal heating have been shown to induce focusing of the heat flux where heating is the most intense (Choblet et al., 2017). We consider here a domain with aspect ratio  $L = 4$  for which the volume production of heat  $q$  takes the form

$$q(x) = 1 - \Delta q \cos\left(\frac{2\pi}{L}x\right) \quad (39)$$

326

327

328

329

330

which is such that the mean heat production is unchanged compared the homogeneous case and the maximum heat production is located at the centre of the domain. In the following, we only illustrate heat modulation with  $\Delta q = 0.5$  in the case of the boundary condition BC 2.  $\Delta q = 0.5$  is a good proxy for tidal heating which bears latitudinal and longitudinal variations by about a factor 2 between minima and maxima.

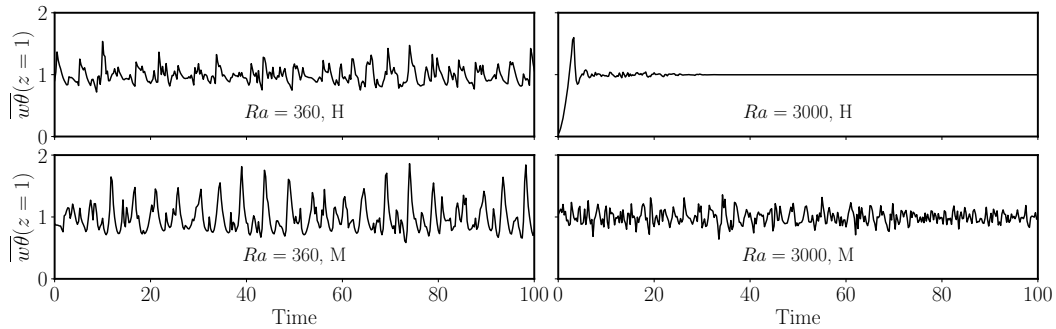


**Figure 10.** Horizontally averaged advective heat flux at the top boundary at  $Ra = 360$  (**left**) and  $Ra = 3000$  (**right**), with comparison between homogeneous (**top**, H) and heterogeneous (**bottom**, M).

331

## 5.2 Large scale flow and pulsatility

332

333

334

335

336

337

338

339

340

341

The large-scale modulation of internal heating leads to the emergence of several striking features. The first one is the attraction of plumes towards the centre where the heating is the most intense. Although plumes may exist in the whole interior of the domain, they merge towards the centre, which results in a higher temperature region with larger heat flux anomaly, as illustrated in figure 9. Plume merging towards the centre is associated with a large-scale mean flow that is also shown in figure 9. Note that at high Rayleigh number ( $Ra = 3000$  in the snapshot of figure 9), small-scale plumes persist in the time-averaged flow. Despite strong variability where heat production is maximal, some plumes remain locked in the areas where heat production is minimal, a feature that is reminiscent of the steady plumes of the homogeneous case.

342

343

344

345

346

347

348

349

350

351

Advection of the plumes towards the largest internal heating region and the subsequent plume merging leads to pulsatility in the advective heat flux, as shown in figure 10. At intermediate Rayleigh number ( $Ra = 360$ ), the flux is intermittent for homogeneous heating but it exhibits a quasi-periodic behaviour for a modulated heating. The typical period is of order one, *i.e.* it takes place over a convective time scale, and corresponds to the time needed for plume formation, advection towards the centre and merging. The effects of heterogeneous heating are even more striking at high  $Ra$ : the steady state observed in the homogeneous case is replaced by quick oscillations of the heat flux (see figure 10). They are due to the many plumes observed in the centre of the domain reaching the top boundary non synchronously (see figure 9).

352

## 5.3 Similarities with the homogeneous-heating case

353

354

355

356

357

358

359

Despite the existence of a mean flow and the pulsatile behaviour detailed in the preceding section, convection with heterogeneous internal heating bears many similarities with the homogeneous case. As already noticed earlier, small scale plumes are still present in the flow, and their typical width remains proportional to  $Ra^{-1/2}$  (see figure 11) but with increased temporal and spatial variability. This means that the balance between horizontal diffusion, heat production and vertical advection is still at play to determine the single plume dynamics.

360

361

362

Moreover, even if lateral variations of the mean temperature are obvious in figure 9, the horizontally averaged temperature follows a trend that is very close to the homogeneous case, as shown in 11. This observation suggests that the spatial form of heat-

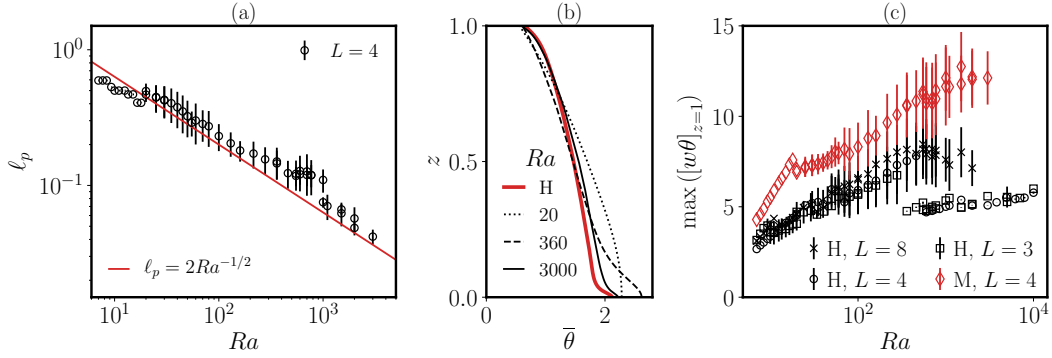


**Figure 11.** (a) Typical plume size in the heterogeneous heating case, and comparison with the same law  $\ell_p \propto Ra^{-1/2}$  as in figure 6. The errorbars are determined in the same way as in figure 6. (b) Mean temperature profile for heterogeneous heating at several Rayleigh numbers; the red line correspond to the temperature profile in the homogeneous case in the high  $Ra$  regime. (c) Maximum value of the non-dimensional advective heat flux at the top of the porous layer determined from the simulations with BC 2. The error bar accounts for the standard deviation of the maximum value over the course of a simulation. Both homogeneous ( $\Delta q = 0$ , labelled H) and heterogeneous ( $\Delta q = 0.5$ , labelled M) are shown.

363 ing is not particularly important for the mean dynamics and scaling laws governing heat  
 364 transport in an internally heated porous medium.

#### 365 5.4 Hydrothermal velocity driven in the ocean

To conclude this theoretical analysis of internally heated porous convection, we derive a scaling law for the hydrothermal velocity driven by the hot plumes in the porous medium as they cross the upper boundary into the ocean above. To evaluate the typical velocity of the buoyant hot water coming out of the core at the bottom of the ocean we must first determine the buoyancy flux associated with the porous plumes. The first question that arises concerns the transposition of the plumes observed in the present model to a three-dimensional geometry, as upwellings may take the form of isolated plumes or ascending sheets. Although there is not a clear theoretical argument in favour of one or the other, several studies point towards the formation of sheets. Monnereau and Dubuffet (2002) has shown in viscous convection that the opening of the top boundary leads to a transition from plumes to sheets. In porous flows, sheet-like convection is observed in simulations of hydrothermal flows (Rabinowicz et al., 1998), and, in particular, in the model of Choblet et al. (2017) for the core of Enceladus. Therefore, we assume in the following that upwelling in the porous medium takes the form of sheets. As in the two-dimensional case, their typical extent is  $Ra^{-1/2}$  because it remains set by the balance between vertical advection, horizontal diffusion and heat production given in equation (27). At the bottom of the ocean, the sheets produce a line source of buoyancy flux  $B$  which drives hydrothermal velocities  $U_h$  of order  $B^{1/3}$ . (Morton et al., 1956; Woods, 2010). The dimensional buoyancy flux is given by (Woods, 2010)

$$B = \int_{\text{upwelling}} \alpha g (\Theta W)|_{z=h} dx, \quad (40)$$

where the one-dimensional integral is computed across an upwelling zone of typical extent  $\ell_p \propto Ra^{-1/2}$ . As  $\Theta$  and  $W$  are proportional to  $Ra$ ,  $B$  scales like  $Ra^{3/2}$ , or more

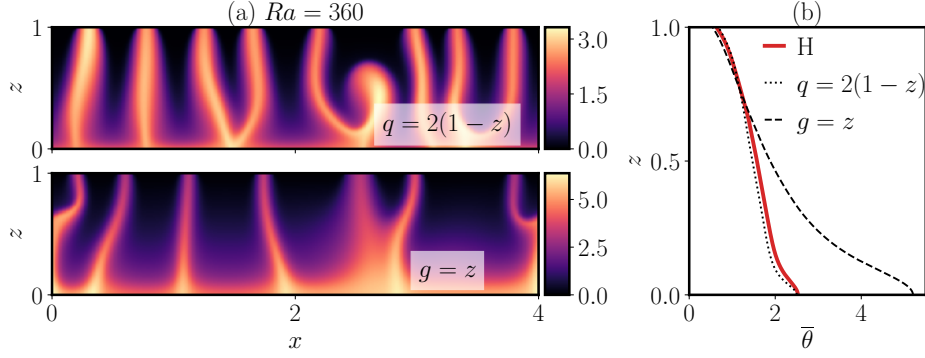


**Figure 12.** (a) Snapshots of the temperature field taken in the statistically steady state of simulations with  $Ra = 360$ . In the upper one, the dimensionless heat production rate is a decreasing function of height  $q = 2(1 - z)$  whereas in the lower one, the dimensionless gravity is a linear function of height  $g = 2z$ . (b) Superposition of the average temperature profiles at  $Ra = 360$  for the homogeneous heating (H), height-dependent heating and height-dependent gravity cases.

explicitly,

$$B \simeq \frac{\kappa^2 \nu}{kh} Ra^{3/2} (w\theta)|_{z=h} \quad \text{and} \quad U_h = \left( \frac{\kappa^2 \nu}{kh} (w\theta)|_{z=h} \right)^{1/3} Ra^{1/2} \quad (41)$$

where we have used the velocity and temperature scales defined in equation (12). Focusing of the heat flux in narrow upwelling zones leads to enhanced values of  $(w\theta)|_{z=h}$ , as shown in figure 11c. In the case of heterogeneous heating, focusing increases the heat flux at the bottom of the ocean by about a factor of 10 over the range of Rayleigh numbers considered here.

## 6 Application of the idealised study to the case of Enceladus

### 6.1 From a two-dimensional model to a planetary core.

To carry out our idealised study of internally heated porous convection, we have discarded many ingredients that will be important for Enceladus, as stated prior to the introduction of the model (section 2.1). Before applying our results, we review these approximations and evaluate how they may affect the conclusions drawn from the two-dimensional Cartesian model.

#### *Sphericity*

First, the definition of the velocity, temperature and time scales as well as the Rayleigh number defined in section 2.3 rely entirely on dimensional analysis and are thus insensitive to the geometry. The dimensionless equations (14) thus take the same expression in any geometry. The critical Rayleigh number above which convection takes place will, presumably, be modified by the geometry, although (Choblet et al., 2017) found convective flows down to  $Ra \simeq 8$  in simulations in a spherical geometry, which puts an upper bound on  $Ra_c$  that is similar to what we find in a Cartesian geometry.

387 We expect that the typical size of upwellings will retain a  $Ra^{-1/2}$  scaling in spher-  
 388 ical geometry, because the balance in (27) that gives this scaling remains the same: lat-  
 389 eral second derivatives must be of order  $Ra$  for orthoradial diffusion to be in balance with  
 390 heat production and radial advection. As a consequence, our prediction for the typical  
 391 buoyancy-flux and hydrothermal-velocity scales should still hold in a spherical geome-  
 392 try.

393 Nevertheless, there will inevitably be differences between the flow in a Cartesian  
 394 and spherical geometry. For example, the ratio of surface area to volume is different, which  
 395 affects the energy-conservation equation for the time-averaged radial heat flux  $\nabla \cdot (\bar{J}(r)\mathbf{e}_r) =$   
 396  $1$  (cf. equation 24). This constraint imposes  $\bar{J}(r) = r/3$ , and the volume-averaged heat  
 397 flux becomes  $\langle J \rangle = 1/6$ , which is a factor 3 smaller than in a Cartesian geometry. As  
 398 a consequence, we expect heat-flux anomalies to either have lower amplitudes or be sparser.  
 399 This simple analysis suggests that the Cartesian geometry might give an upper bound  
 400 on the buoyancy flux and the hydrothermal velocity induced in the ocean compared to  
 401 the real spherical case.

402

### 403 *Depth-dependence of heat production and gravity*

404 The model developed here also neglects any vertical variations of gravity and vol-  
 405 umetric heat production, and we briefly explore their possible importance here with the  
 406 aid of a few additional simulations. Volumetric heat production on Enceladus decreases  
 407 away from the center to become negligible close to the surface (Choblet et al., 2017), but  
 408 the decreases remains sufficiently slow for the shell-average heat production to increase  
 409 with radius. In the uniform heating case, we have found that the structure of the flow  
 410 is governed by a local balance between advection, diffusion and volumetric heat produc-  
 411 tion. We anticipate such a balance to remain at play when heat production varies with  
 412 depth which makes the volumetric heating variations more relevant to the dynamics than  
 413 those of the shell-average heating. Therefore, to test the effect of vertical variations of  
 414 heat production, we have carried out simulations with a decreasing source term  $q(z) =$   
 415  $2(1-z)$  in the advection-diffusion equation that retains the same spatial average as in  
 416 the uniform case. A typical snapshot is shown in figure 12 along with the mean verti-  
 417 cal temperature profile,  $\bar{\theta}$ . They both show very little difference from the uniform-heating  
 418 case (see figure 3), suggesting that vertical variation in heat-production does not play  
 419 an important dynamical role, at least in Cartesian geometry.

420

421 The picture is slightly changed when we consider uniform heating but with a depth-  
 422 dependent gravitational field. In a uniform-density planetary core, we expect  $g$  to increase  
 423 linearly with radius, and so we carried out a few example simulations in which the di-  
 424 mensionless gravity is  $g = z$  (i.e. gravity is normalised by its surface value). The ef-  
 425 fect of this on the equations is to add a factor of  $z$  in front of the temperature in the di-  
 426 mensionless version of Darcy's law (see equation (14)). A snapshot of the temperature  
 427 field (figure 12) reveals that plumes are narrower and less numerous than in the homo-  
 428 geneous case. As a consequence, the maximum advective flux carried by the plumes is  
 429 roughly double that of the homogeneous case. The average temperature profile is also  
 430 strikingly different: weaker gravity at depth makes advection inefficient as a means of  
 431 evacuating heat, resulting in larger temperature at the bottom of the domain. However,  
 432 because plumes are thinner, lateral diffusion is enhanced and the plume temperature de-  
 433 creases as they rise. As a consequence, the hot-spot temperature at the upper surface  
 remains similar to the modulated case, *i.e.*  $\max(\theta(z=1)) \sim 4$ .

434

435 Note that the variations with  $z$  of gravity and heat production do not affect the  
 436 scaling  $Ra^{-1/2}$  governing the size of the plumes (and hence the hydrothermal velocity).  
 437 Since the dimensionless gravity and volumetric heating remain at most order 1, the bal-  
 ance between horizontal diffusion, heat production and vertical advection still holds in

Core radius ( $h$ )	186 km
Water density ( $\rho_0$ )	$1.0 \times 10^3 \text{ kg.m}^{-3}$
Matrix density ( $\rho_m$ )	$2.8 \times 10^3 \text{ kg.m}^{-3}$
Water heat capacity ( $c_0$ )	$4.1 \times 10^3 \text{ J.K}^{-1}.\text{kg}^{-1}$
Matrix heat capacity ( $c_m$ )	$1.0 \times 10^3 \text{ J.K}^{-1}.\text{kg}^{-1}$
Water conductivity ( $\lambda_0$ )	$0.6 \times 10^3 \text{ W.K}^{-1}.\text{m}^{-1}$
Matrix conductivity ( $\lambda_m$ )	$2.8 \times 10^3 \text{ W.K}^{-1}.\text{m}^{-1}$
Water thermal expansion ( $\alpha$ )	$1.2 \times 10^{-3} \text{ K}^{-1}$
Kinematic viscosity ( $\nu$ )	$1 \times 10^{-6} \text{ m}^2.\text{s}^{-2}$
Thermal diffusivity ( $\kappa$ )	$6 \times 10^{-7} \text{ m}^2.\text{s}^{-2}$
Porosity ( $\varphi$ )	0.20
Gravity ( $g$ )	$0.1 \text{ m.s}^{-2}$

**Table 2.** A summary of the bulk physical parameters used to transpose our idealised study to the case of Enceladus’ core, adapted from (Choblet et al., 2017) (see in particular the Supplementary Material of that paper). Note that the modified porosity is  $\bar{\varphi} = 0.76$ .

438 the same way as in the uniform case. In fact, the asymptotic expansion of section 4.5  
 439 can be reworked with  $z$ -dependent gravity and volumetric heating down to equation (31)  
 440 without affecting the hierarchy between each term. Therefore, the scaling laws we have  
 441 derived in the preceding sections are robust to these additional physical ingredients.

442 We also briefly considered the effect of depth-dependence in the modulation am-  
 443 plitude  $\Delta q$  for the results presented in section 5, since the modulation should increase  
 444 with depth, being almost negligible near the core (Choblet et al., 2017). We carried out  
 445 simulations with  $\Delta q = z$ , which retains the same average modulation as previously. Re-  
 446 sults showed little change from those discussed in section 5: a mean flow drags small-  
 447 scale plumes towards the areas with larger volumetric heating which causes the flow to  
 448 be unsteady. The strong pulsatility with bursts of heat flux observed at  $Ra = 360$  in  
 449 figure 10 are weaker, however, with the time series of  $\overline{w\theta}(z = 1)$  being more similar to  
 450 the homogeneous case.

## 451 **6.2 Quantification of convection in Enceladus’ core**

452 The preceding discussion suggests that the simplified two-dimensional Cartesian  
 453 model of internally heated porous convection produces scaling laws, at least in terms of  
 454 orders of magnitude, provide a reasonable description of the flow and the hydrothermal  
 455 activity inside icy moons. Here we apply our results to Enceladus.

### 456 ***Physical properties of Enceladus’ core***

457 To characterise convection inside Enceladus’ core, and to compare our results to  
 458 existing literature, we use the same physical parameters as in (Choblet et al., 2017). A  
 459 set of fixed physical constants that are relevant to characterise heat transport are given  
 460 in table 2. We reproduce the process used in (Choblet et al., 2017) and do not precisely  
 461 specify the permeability  $k$  and internal heat production  $Q_V$  values on which the uncer-  
 462 tainty is the largest. Instead, we consider that  $k$  may range from  $10^{-15} \text{ m}^2$  to  $10^{-12} \text{ m}^2$   
 463 and that the tidal heating is between 10 GW and 40 GW. (The lower bound is directly  
 464 inferred from the heat flux measurement at the South Pole of Enceladus (Spencer et al.,  
 465 2006, 2018).) Therefore, we draw maps of the behaviour of the system keeping the pa-  
 466 rameters of table 2 constant and varying both  $k$  and  $Q_V$ .

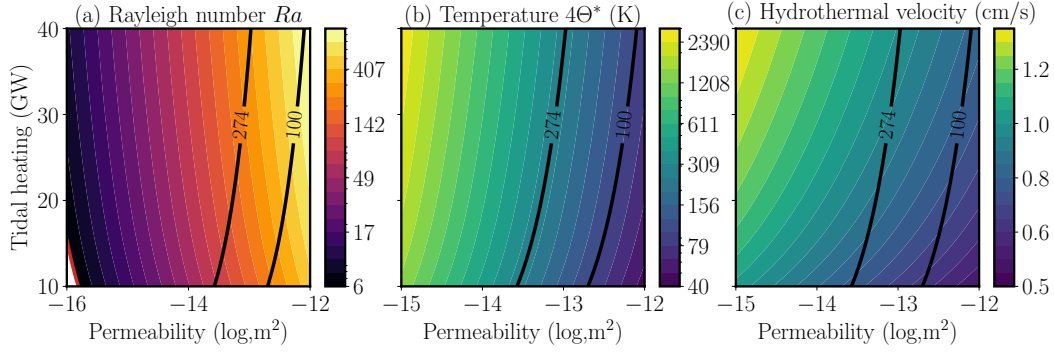


**Figure 13.** (a) the Rayleigh number as a function of the permeability and the tidal heating. The red line marks the onset of convection for the homogeneous heating case. (b) Typical maximum dimensional temperature  $4\Theta^*$  (in Kelvin) (see (42)) inside the porous core of Enceladus. (c) Typical hydrothermal velocity obtained from the buoyancy flux at the bottom of the ocean as a function of permeability and tidal heating. On each panel, the 274 K isotherm gives the liquid-vapour transition at the hydrostatic pressure of core–ocean boundary, which represents a rough upper bound on the temperature for the model to remain valid with respect to phase change. The 100 K isotherm gives an estimate of the maximum temperature derived from geochemical measurements (Sekine et al., 2015; Hsu et al., 2015).

467

### *The Rayleigh number inside Enceladus*

468

469

470

471

472

473

As explained in section 2.3, the overall behaviour of the system depends only on one dimensionless parameter, the Rayleigh number, defined in (13), which is a power law of both  $k$  and  $Q_V$ . The map of the possible values of the Rayleigh number inside the core of Enceladus is given in figure 13. In the range of values of  $k$  considered in (Choblet et al., 2017), the system is always unstable to convection, although  $Ra$  does not reach very high values and remains below 1000.

474

475

### *Maximum temperature*

We have shown in section 4.3 that heat transport is mostly advective, even at values of the Rayleigh number that are close to the onset of the instability. In such a regime, the dimensionless temperature takes  $O(1)$  values, with a maximum of about 4 in the case of horizontally modulated heat production (see for instance the snapshots of figure 9) in reached at the core of the plumes. Hence,  $4\Theta^*$  is a good proxy for the maximum temperature difference between the ocean and the core of Enceladus, with  $\Theta^*$  the temperature scale defined in section 2.3,

$$\Theta^* = \frac{\kappa\nu}{k\alpha gh} Ra . \quad (42)$$

476

477

The maximum temperature difference  $4\Theta^*$  is shown in figure 13 and, depending on the parameters, it ranges from 40 K to 3000 K.

478

479

480

481

482

The computation of the maximum temperature difference allows us to determine the limit of validity of our model which does not include phase change of water from liquid into vapor. On the one hand, according to the snapshots of figures 3 and 9, the core temperature of plumes is almost constant with height. On the other hand, the boiling point of water is an increasing function of pressure and depth. As a consequence, the max-

imum temperature temperature allowed in our model is given by the boiling point of water at the core–ocean boundary. Assuming that the core lies below 60 km of liquid and solid water with density  $1 \times 10^3 \text{ kg.m}^{-3}$  and constant gravity, a crude estimate for the pressure is 6 Mpa at the core–ocean boundary. The corresponding boiling point for pure water is 547 K (Haynes, 2012). If we assume the ocean to be well-mixed and made of pure water, its averaged temperature should be similar to the fusion temperature of ice, that is, 273 K (Haynes, 2012). Hence, we show in figure 13 the isotherm 274 K which gives a crude upper bound on the validity of the single-phase model that is used here and in the literature dealing with internal models of icy moons, although other additional ingredients (composition, variable gravity) may shift this upper bound in a way that remains to be determined.

Note that Hsu et al. (2015) have shown via the ice plume composition that the water flowing inside Enceladus has been in contact with rocks at a temperature of about  $90^\circ \text{ C}$ . We show in figure 13 the location of where the maximum temperature difference reaches 100 K which roughly corresponds to this important constraint on the maximum temperature. Our idealised model suggests a constraint on the permeability of Enceladus’ core of  $10^{-13}$  to  $10^{-12} \text{ m}^2$ , for the range of tidal heating considered.

500

### 501 ***Hydrothermal velocity in Enceladus’ ocean***

Using the law (41) governing the buoyancy flux  $B$  driven by porous convection in the ocean, we compute the typical hydrothermal velocity  $B^{1/3}$  in Enceladus’ ocean. With dimensionless heat flux  $w\theta \sim 10$  in the core of the thermal anomalies, the typical hydrothermal velocity is found to be about 1 cm/s, no matter what the permeability or the tidal heating are (see figure 13c). This value is in agreement with the typical velocity found by (Choblet et al., 2017) with different scaling arguments relying on the power anomaly advected to the ocean floor. As a consequence, for a subsurface ocean whose thickness is of the order 10–30 km (Thomas et al., 2016), the expected turn-over timescale is of the order of a month, at most.

511

### 512 ***Typical velocity and temporal variability***

The typical velocity scale  $U^*$  of the flow in the core is given by a diffusive velocity  $\kappa/h$  augmented by a factor  $Ra$ , that is:

$$U^* = \frac{\kappa}{h} Ra . \quad (43)$$

The diffusive velocity scale amounts to  $0.1 \text{ mm.yr}^{-1}$ , and because  $Ra$  does not exceed  $10^3$ , the Darcy flux remains below  $10 \text{ cm.yr}^{-1}$ . The hydrothermal activity at the bottom of Enceladus’ ocean is therefore very different from the what is commonly observed at the bottom of the Earth’s oceans, where typical Darcy fluxes are rather of the order of a few meters per year ( $10^3$  times larger). This difference is largely due to the much weaker gravitational acceleration in Enceladus.

518

Consequently, the convective time scale  $\tau$  is:

$$\tau = \frac{h}{\bar{\varphi} U^*} = \frac{h^2}{\bar{\varphi} \kappa} Ra^{-1} \simeq 0.8 \text{ Gy} \times Ra^{-1} , \quad (44)$$

The typical variability timescale, for instance for the flux at the top boundary (see figure 10) is thus at least 1 million years. It is a very slowly evolving system compared to the turnover timescale of the subsurface ocean, or to the timescale of human observations. In our simulations, we have observed bursts in the convective activity that give rise to a 40-50% increase in the average heat flux at the surface of the core that may last

523

524 for a few million years. These bursts correspond to more active plumes that would cause  
 525 enhanced hydrothermal activity inducing preferential erosion of the ice shell above. One  
 526 may thus speculate that, in the past, intense plumes similar to the one at the south pole  
 527 of Enceladus could have been active at other locations. Such a hypothesis might explain  
 528 the existence of older tectonised terrains at the surface of Enceladus (Crow-Willard &  
 529 Pappalardo, 2015). Lastly, localised bursts could also be at the start of the runaway mech-  
 530 anism proposed by (Choblet et al., 2017) to explain the asymmetry between the north  
 531 and south poles of Enceladus: a thinner ice crust locally enhances tidal heating, which  
 532 in turns enhances ice erosion.

## 533 7 Conclusion and discussion

534 Throughout this article, we have explored heat transport in a fluid-saturated, in-  
 535 ternally heated porous medium with an idealised Cartesian model. Our set-up is based  
 536 on an idealisation of the model of Choblet et al. (2017) describing the tidally-driven hy-  
 537 drothermal activity in the interior of Enceladus. The behaviour of the system is governed  
 538 by a single dimensionless number, the Rayleigh number  $Ra$ , which is an increasing func-  
 539 tion of both the permeability and the internal heat production. With the combination  
 540 of numerical simulations and mathematical analysis, we have derived general laws gov-  
 541 erning hydrothermal activity driven by volumetric heating.

542 We have shown that heat transport in the porous medium is governed by advec-  
 543 tion. In this regime, the temperature difference between the porous matrix and the pure  
 544 fluid ocean scales like  $Ra$ . This scaling enables use to constrain the plausible range of  
 545 values for the permeability of Enceladus' core. According to Hsu et al. (2015), the tem-  
 546 perature scale should be at most 100 K. For values of tidal heating that are consistent  
 547 with the heat flux measurement at the surface of Enceladus, our scaling indicates that  
 548 the permeability should be around  $10^{-13} - 10^{-12} \text{ m}^2$ .

549 In our simulations, we have reproduced the observation drawn from the simulations  
 550 of Choblet et al. (2017) that the upwelling zones tend to narrow as the Rayleigh num-  
 551 ber is increased, and that they concentrate where internal heating is the most intense.  
 552 Our simulations show that the typical plume size follows a  $Ra^{-1/2}$  power law, which is  
 553 imposed by a balance between vertical advection and horizontal diffusion of heat. This  
 554 law governing the size of heat flux anomalies at the bottom of the ocean of Enceladus  
 555 compels the typical buoyancy flux injected into the ocean to be proportional to  $Ra^{3/2}$ .  
 556 Over the range of tidal heating and permeability that are consistent with observational  
 557 data, we have found that the typical hydrothermal velocity in the ocean of Enceladus  
 558 is about 1 cm/s. Despite the idealisation of our model, such an estimate is consistent with  
 559 the one derived by Choblet et al. (2017) from an estimate of a typical heat flux anomaly.  
 560 The model used here has also helped us to highlight the underpinning of heat transport  
 561 in an internally heated porous layers. In particular, we have shown that the heat-transport  
 562 efficiency, which has been characterised via a generalised Nusselt number, has the same  
 563 scaling as the classical Rayleigh-Bénard convection in porous media (Otero et al., 2004;  
 564 Hewitt et al., 2012, 2014).

565 Despite the highly idealised nature of our approach, we have argued that the scal-  
 566 ing laws found for the typical size of thermal anomalies, the time-variability and the hy-  
 567 drothermal activity are also expected in spherical geometry, and are robust to the in-  
 568 clusion of additional ingredients such as vertical variations of heat production and grav-  
 569 ity. These scaling laws could thus be applied to the other small icy moons of the Solar  
 570 System, in particular those of Saturn's E ring, whose internal structure is similar to Ence-  
 571 ladus' (Nimmo & Pappalardo, 2016). Although Enceladus is the only one showing signs  
 572 of present internal activity, these other bodies could have been active in the past. Our  
 573 study thus paves the way for more systematic understanding of the thermal evolution  
 574 of these bodies. It could also apply to larger icy moons such as Europa where the ocean  
 575 is in contact with a rocky mantle that is internally heated by radiogenic decay.

576 Of course, the simple scaling arguments contained here are not a substitute for a  
 577 detailed investigation of the idealised problem in a spherical geometry, which would be  
 578 a useful future extension to this work. Such a study would give a clearer picture of the  
 579 flow structures in a spherical geometry, as well providing more quantitative predictions  
 580 of hot-spot widths, time-variability and strength. Beyond these geometrical considera-  
 581 tions, there are also other effects that have not been discussed here or in the existing lit-  
 582 erature that could lead to significant changes in convective heat transport. One ma-  
 583 jor simplification of all models of porous planetary interiors is the assumption of homo-  
 584 geneous and isotropic permeability  $k$ . Since the core of small icy satellites such as Ence-  
 585 lадus' is an aggregate of heterogeneous material, their permeability is unlikely to be uni-  
 586 form. It is not even clear whether coarse-grained modelling based on the assumption of  
 587 strong confinement, that is, Darcy's law, is entirely relevant for the core of icy satellites,  
 588 although, as we've seen, Darcy's law with small permeability is consistent with observed  
 589 data. However, we do not believe any significant progress can be achieved in these di-  
 590 rections without further constraining the core's small-scale structure.

591 In addition, the model we consider completely discards flows that are directly driven  
 592 by the periodic tidal distortion. Although the tidal deformation field is purely incom-  
 593 pressible in continuous media, mean flows analogous to Stokes drift may result from the  
 594 periodic motion of the porous matrix. Whether deformation-driven flows are compara-  
 595 ble to buoyancy-driven flows remains to be quantified.

596 Lastly, there is a need to clarify the behaviour of the system at the top of the porous  
 597 core and the coupling between the porous layer and the above ocean. We have stated  
 598 in the second section that the two possible thermal boundary conditions used here (im-  
 599 posed temperature or free temperature in the upwellings) are the two end-members of  
 600 the behaviour of the fluid at the interface. The imposed temperature condition could rep-  
 601 resent a very slow porous layer lying underneath a very well mixed ocean. This situa-  
 602 tion could be relevant to the case of Enceladus and other icy moons as the Darcy flux  
 603 ( $\sim 1 \text{ cm.yr}^{-1}$ ) is very small compared to the hydrothermal velocity ( $\sim 1 \text{ cm.s}^{-1}$ ). In  
 604 this configuration, the water coming out of the core is at the same temperature as the  
 605 ocean and is neutrally buoyant; there is then no hydrothermal activity in the sense of  
 606 what we know at the bottom of the Earth's ocean. Nevertheless, it is associated to a dif-  
 607 fusive heat flux anomaly on the subsurface ocean's floor which is likely to drive convec-  
 608 tion and mixing in the ocean. The observed chemical signature of contact with silicate  
 609 rocks at high temperature (Hsu et al., 2015) could very well happen below the thin ther-  
 610 mal boundary layer at the top of the core. Moreover, current thermal evolution mod-  
 611 els of icy moons rely on parametrisation of hydrothermally-driven convection in the sub-  
 612 surface ocean that are based on the classical Rayleigh-Bénard problem (Travis et al., 2012;  
 613 Travis & Schubert, 2015). It is, however, not clear at all whether such parametrisation  
 614 actually applies to the present system where ocean convection is driven by strong and  
 615 localised heterogeneities of either the advective or the diffusive heat flux at the bottom  
 616 boundary. In short, it remains difficult to produce a definitive statement about the ther-  
 617 mal structure of the subsurface ocean without a careful study of the coupled system with  
 618 two very different typical evolution timescales for each medium.

## 619 Acknowledgments

620 The authors acknowledge support from the 2018 WHOI GFD program, supported by  
 621 the US National Science Foundation (award no. 1332750) and the Office of Naval Re-  
 622 search, where most of this research was carried out. TLR is supported by the Royal So-  
 623 ciety through a Newton International Fellowship (Grant reference NIF\R1\192181). The  
 624 source codes and output data are available on Figshare (Le Reun & Hewitt, 2020).

## References

- Buretta, R. J., & Berman, A. S. (1976, June). Convective Heat Transfer in a Liquid Saturated Porous Layer. *Journal of Applied Mechanics*, *43*(2), 249–253. doi: 10.1115/1.3423818
- Choblet, G., Tobie, G., Sotin, C., Běhouňková, M., Čadek, O., Postberg, F., & Souček, O. (2017, November). Powering prolonged hydrothermal activity inside Enceladus. *Nature Astronomy*, *1*. doi: 10.1038/s41550-017-0289-8
- Coumou, D., Driesner, T., & Heinrich, C. A. (2008, September). The Structure and Dynamics of Mid-Ocean Ridge Hydrothermal Systems. *Science*, *321*(5897), 1825–1828. doi: 10.1126/science.1159582
- Coumou, D., Driesner, T., Weis, P., & Heinrich, C. A. (2009, March). Phase separation, brine formation, and salinity variation at Black Smoker hydrothermal systems. *Journal of Geophysical Research*, *114*(B3). doi: 10.1029/2008JB005764
- Crow-Willard, E. N., & Pappalardo, R. T. (2015). Structural mapping of Enceladus and implications for formation of tectonized regions. *Journal of Geophysical Research: Planets*, *120*(5), 928–950. doi: 10.1002/2015JE004818
- Cserepes, L., & Lenkey, L. (2004, August). Forms of hydrothermal and hydraulic flow in a homogeneous unconfined aquifer. *Geophysical Journal International*, *158*(2), 785–797. doi: 10.1111/j.1365-246X.2004.02182.x
- Drazin, P. G. (2002). *Introduction to Hydrodynamic Stability*. Cambridge University Press.
- Fontaine, F. J., & Wilcock, W. S. D. (2007, July). Two-dimensional numerical models of open-top hydrothermal convection at high Rayleigh and Nusselt numbers: Implications for mid-ocean ridge hydrothermal circulation: HYDROTHERMAL CONVECTION. *Geochemistry, Geophysics, Geosystems*, *8*(7), n/a-n/a. doi: 10.1029/2007GC001601
- Goluskin, D. (2016). A Family of Convective Models. In *Internally Heated Convection and Rayleigh-Bénard Convection* (pp. 1–26). Springer, Cham. doi: 10.1007/978-3-319-23941-5\_1
- Hardee, H. C., & Nilson, R. H. (1977, June). Natural Convection in Porous Media with Heat Generation. *Nuclear Science and Engineering*, *63*(2), 119–132. doi: 10.13182/NSE77-A27015
- Haynes, W. M. (2012). *CRC Handbook of Chemistry and Physics, 93rd Edition*. CRC Press.
- Hewitt, D. R., & Lister, J. R. (2017, October). Stability of three-dimensional columnar convection in a porous medium. *Journal of Fluid Mechanics*, *829*, 89–111. doi: 10.1017/jfm.2017.561
- Hewitt, D. R., Neufeld, J. A., & Lister, J. R. (2012, May). Ultimate Regime of High Rayleigh Number Convection in a Porous Medium. *Physical Review Letters*, *108*(22), 224503. doi: 10.1103/PhysRevLett.108.224503
- Hewitt, D. R., Neufeld, J. A., & Lister, J. R. (2014, October). High Rayleigh number convection in a porous medium containing a thin low-permeability layer. *Journal of Fluid Mechanics*, *756*, 844–869. doi: 10.1017/jfm.2014.478
- Hsu, H.-W., Postberg, F., Sekine, Y., Shibuya, T., Kempf, S., Horányi, M., ... Srama, R. (2015, March). Ongoing hydrothermal activities within Enceladus. *Nature*, *519*(7542), 207–210. doi: 10.1038/nature14262
- Kulacki, F. A., & Ramchandani, R. (1975, September). Hydrodynamic instability in a porous layer saturated with a heat generating fluid. *Wärme- und Stoffübertragung*, *8*(3), 179–185. doi: 10.1007/BF01681559
- Lainey, V., Jacobson, R. A., Tajeddine, R., Cooper, N. J., Murray, C., Robert, V., ... Zahn, J.-P. (2017, January). New constraints on Saturn’s interior from Cassini astrometric data. *Icarus*, *281*, 286–296. doi: 10.1016/j.icarus.2016.07.014
- Le Reun, T., & Hewitt, D. R. (2020, May). *Internally heated porous convection: An idealised model for Enceladus’ hydrothermal activity*. doi: 10.6084/m9.figshare.11973591.v2

- 680 Monnereau, M., & Dubuffet, F. (2002, August). Is Io's Mantle Really Molten?  
681 *Icarus*, 158(2), 450–459. doi: 10.1006/icar.2002.6868
- 682 Morton, B. R., Taylor, G. I., & Turner, J. S. (1956, January). Turbulent gravi-  
683 tational convection from maintained and instantaneous sources. *Proc. R. Soc.*  
684 *Lond. A*, 234(1196), 1–23. doi: 10.1098/rspa.1956.0011
- 685 Nield, D. A., & Bejan, A. (2013). Heat Transfer Through a Porous Medium. In  
686 D. A. Nield & A. Bejan (Eds.), *Convection in Porous Media* (pp. 31–46). New  
687 York, NY: Springer. doi: 10.1007/978-1-4614-5541-7\_2
- 688 Nield, D. A., & Kuznetsov, A. V. (2013, July). Onset of Convection with Internal  
689 Heating in a Weakly Heterogeneous Porous Medium. *Transport in Porous Me-*  
690 *dia*, 98(3), 543–552. doi: 10.1007/s11242-013-0158-6
- 691 Nimmo, F., & Pappalardo, R. T. (2016). Ocean worlds in the outer solar sys-  
692 tem. *Journal of Geophysical Research: Planets*, 121(8), 1378–1399. doi:  
693 10.1002/2016JE005081
- 694 Otero, J., Dontcheva, L. A., Johnston, H., Worthing, R. A., Kurganov, A., Petrova,  
695 G., & Doering, C. R. (2004, January). High-Rayleigh-number convection in a  
696 fluid-saturated porous layer. *Journal of Fluid Mechanics*, 500, 263–281. doi:  
697 10.1017/S0022112003007298
- 698 Press, W. H., Teukolsky, S. A., Vetterling, W. T., & Flannery, B. P. (1992). *Nu-*  
699 *merical recipes in FORTRAN* (2nd ed ed.). Cambridge [England] ; New York:  
700 Cambridge University Press.
- 701 Rabinowicz, M., Boulègues, J., & Genthon, P. (1998, October). Two- and three-  
702 dimensional modeling of hydrothermal convection in the sedimented Middle  
703 Valley segment, Juan de Fuca Ridge. *Journal of Geophysical Research: Solid*  
704 *Earth*, 103(B10), 24045–24065.
- 705 Roberts, J. H. (2015, September). The fluffy core of Enceladus. *Icarus*, 258, 54–66.  
706 doi: 10.1016/j.icarus.2015.05.033
- 707 Sekine, Y., Shibuya, T., Postberg, F., Hsu, H.-W., Suzuki, K., Masaki, Y., ... Sirono,  
708 S.-i. (2015, October). High-temperature water–rock interactions and hy-  
709 drothermal environments in the chondrite-like core of Enceladus. *Nature*  
710 *Communications*, 6(1), 1–8. doi: 10.1038/ncomms9604
- 711 Souček, O., Kalousová, K., & Čadek, O. (2014, November). Water trans-  
712 port in planetary ice shells by two-phase flow – a parametric study. *Geo-*  
713 *physical & Astrophysical Fluid Dynamics*, 108(6), 639–666. doi: 10.1080/  
714 03091929.2014.969251
- 715 Spencer, J. R., Nimmo, F., Ingersoll, A. P., Hurford, T. A., Kite, E. S., Rhoden,  
716 A. R., ... Howett, C. J. A. (2018). Plume Origins and Plumbing: From Ocean  
717 to Surface. In P. M. Schenk, R. N. Clark, C. J. A. Howett, A. J. Verbiscer,  
718 & J. H. Waite (Eds.), *Enceladus and the Icy Moons of Saturn* (pp. 163–174).  
719 Tucson, AZ: University of Arizona Press.
- 720 Spencer, J. R., Pearl, J. C., Segura, M., Flasar, F. M., Mamoutkine, A., Romani, P.,  
721 ... Lopes, R. M. C. (2006, March). Cassini Encounters Enceladus: Background  
722 and the Discovery of a South Polar Hot Spot. *Science*, 311(5766), 1401–1405.  
723 doi: 10.1126/science.1121661
- 724 Thomas, P. C., Tajeddine, R., Tiscareno, M. S., Burns, J. A., Joseph, J., Loredó,  
725 T. J., ... Porco, C. (2016, January). Enceladus's measured physical li-  
726 bration requires a global subsurface ocean. *Icarus*, 264, 37–47. doi:  
727 10.1016/j.icarus.2015.08.037
- 728 Travis, B. J., Palguta, J., & Schubert, G. (2012, April). A whole-moon thermal his-  
729 tory model of Europa: Impact of hydrothermal circulation and salt transport.  
730 *Icarus*, 218(2), 1006–1019. doi: 10.1016/j.icarus.2012.02.008
- 731 Travis, B. J., & Schubert, G. (2015, April). Keeping Enceladus warm. *Icarus*, 250,  
732 32–42. doi: 10.1016/j.icarus.2014.11.017
- 733 Woods, A. W. (2010, January). Turbulent Plumes in Nature. *Annual Review of*  
734 *Fluid Mechanics*, 42(1), 391–412. doi: 10.1146/annurev-fluid-121108-145430